Imaging transverse modes in a gigahertz surface-acoustic-wave cavity

M. Fisicaro,* T.A. Steenbergen, Y.C. Doedes, K. Heeck, and W. Löffler
Leiden Institute of Physics, Niels Bohrweg 2, Leiden 2333 CA, Netherlands

(Received 23 August 2024; revised 27 November 2024; accepted 16 December 2024; published 15 January 2025)

Full characterization of surface-acoustic-wave (SAW) devices requires imaging the spatial distribution of the acoustic field, which is not possible with standard all-electrical measurements where an interdigital transducer is used as a detector. Here we present a fiber-based scanning Michelson interferometer employing a strongly focused laser beam as a probe. Combined with a heterodyne circuit, this setup enables frequency- and spatially resolved measurements of the amplitude and phase of the SAW out-of-plane displacement. We demonstrate this by investigating a 1-GHz SAW cavity, revealing the presence of frequency-overlapping transverse modes, which are not resolved with an all-electrical measurement. The frequency overlap of these transverse modes leads to mode superpositions, which we analyze by quadrature decomposition of the complex acoustic field.

DOI: 10.1103/PhysRevApplied.23.014032

I. INTRODUCTION

Surface acoustic waves (SAWs) are mechanical waves that travel along the surface of a material, and they find many applications in modern technologies, due to the ease of excitation on piezoelectric substrates via interdigital transducers (IDTs) [1–3]. For instance, their surface confinement makes them useful in chemical and biological sensing, where a compound placed on the free surface of the piezoelectric material interacts with the propagating waves [4–7], and in the manipulation of biological matter such as cells [8–10]. The small acoustic wavelength at gigahertz frequencies allows for miniaturization of electronic filters, finding applications in telecommunications [11–13]. Because of their long coherence times, and their ability to interact with many different quantum systems, SAWs are also used in quantum physics research, where they can couple to a variety of two-level systems, such as superconducting qubits [14–17], nitrogen-vacancy centers, and quantum dots [18–22]. Many of these applications require spatial confinement of the SAWs, and this can be achieved by patterning periodic gratings (Bragg mirrors) on the surface of the host material [23–26] to obtain an acoustic cavity. A typical configuration is a one-port resonator, consisting of two SAW mirrors enclosing an IDT, which can be simultaneously used for SAW excitation and detection.

The characterization of SAW devices is typically done in the frequency domain with an all-electrical measurement using a vector network analyzer (VNA), which, in the case of a SAW cavity, consists in measuring the acoustic resonance spectrum [27]. This approach does not provide spatial information, which requires imaging the acoustic field distribution in the SAW device, and can be done with different techniques employing an external probe, such as atomic force microscopy [28], X-ray diffraction [29–31], and optical probes [32–37]. Among these, interferometric optical probes stand out for their simple implementation and high sensitivity in displacement measurements [38–42]. Understanding of transverse modes in SAW devices is important, since they often have detrimental effects. In SAW filters, for instance, transverse modes cause ripples in the passband and/or undesirable peaks in the rejection band [12], which can be mitigated by properly shaping the IDT fingers [43,44].

Here we present a fiber-based scanning Michelson interferometer with a heterodyne circuit, combining frequency- and spatially resolved measurements of the amplitude and phase of the SAW out-of-plane displacement. We demonstrate this by investigating a planar-mirror SAW cavity device, operating at 1 GHz. We measure the acoustic resonance spectrum spatially resolved, which reveals spatial superpositions of frequency-overlapping transverse modes that cannot be resolved in all-electrical VNA measurements.

II. EXPERIMENTAL SETUP

A. SAW device

The device investigated in this paper is a planar SAW cavity, as shown in Fig. 1(a). This device has been nanofabricated via electron-beam lithography and

*Contact author: fisicaro@physics.leidenuniv.nl

Published by the American Physical Society under the terms of the Creative Commons Attribution 4.0 International license. Further distribution of this work must maintain attribution to the author(s) and the published article's title, journal citation, and DOI.

electron-beam evaporation of aluminum on a (001)-cut GaAs substrate. It consists of an IDT with 10 metal finger pairs, placed inside a cavity formed by two planar mirrors, each one made of 250 metal fingers. The metal thickness of the IDT and the mirrors is $h = 50$ nm, the center-to-center finger spacing is $p = 1.4$ μm, and the finger width is $d = 700$ nm. The two mirrors are placed at a distance of $L_{\mathrm{cav}} = 470$ μm from each other, and the length of the fingers in the transverse direction is $L_y = 308$ μm. The device is oriented along the [110] direction, for which the speed of the (Rayleigh) surface acoustic wave is $v_{\mathrm{SAW}} \simeq 2860$ m/s, resulting in a wavelength $\Lambda \simeq 2.8$ μm at the frequency $f_{\mathrm{SAW}} = 1.022$ GHz.

B. Fiber-based scanning Michelson interferometer

The optical setup shown in Fig. 1(b) is a scanning Michelson interferometer implemented with a polarization-maintaining single-mode fiber coupler as the beam splitter (PM BS). Light from a narrow-linewidth fiber-coupled laser (TOPTICA DL Pro) with $\lambda = 980$ nm enters the fiber coupler through port A, and is split into the sample (port D) and reference arm (port C). In the reference arm, the light is focused onto a mirror by a single aspheric lens L_1, and back-reflected into the fiber. In the sample arm, light from port D is first collimated by an aspheric lens (L_2), and then strongly focused onto the GaAs-based SAW device by an aspheric lens with numerical aperture 0.55 (L_3), resulting in a spot size of $2w_0 = 2.8$ μm, where w_0 is the beam waist radius.

Because of Fresnel reflection, at $\lambda = 980$ nm, the GaAs surface acts as a partial mirror with reflectivity $R \simeq 0.3$, and the reflected light is coupled back into the fiber coupler through the same port D. The light reflected from the reference and sample arms of the interferometer is then recombined through the same fiber coupler, and exits through port B. After port B, the recombined light is split again by a fiber splitter (30:70 splitting ratio). The weaker part is sent to a slow photodiode (Thorlabs PDA36-EC), the other to a radio-frequency photodiode (New Focus 1514). The slow photodiode (slow PD) is used to generate the error signal used for stabilization of the interferometer (side-of-fringe lock). This signal is first sent to a proportional-integral-derivative (PID) controller, and then to a piezo driver used to actuate the piezo element on which the mirror in the reference arm of the interferometer is attached.

The gigahertz signal detected with the radio-frequency photodiode (Rf PD) is down-converted to an intermediate-frequency signal in the range 1–48 MHz by the heterodyne circuit, and then measured with a lock-in amplifier (Zurich Instruments HF2LI, 50-MHz bandwidth). The origin of the 1-GHz fluctuations in the optical power lies in the interference between the light from the reference arm, and the light from the sample arm of the interferometer, which is phase-modulated at 1 GHz due to the out-of-plane surface displacement associated to the SAWs. In the sample arm of the interferometer, two pellicle beam splitters redirect part of the back-reflected light to a CCD, used to image and align the SAW device, and to a reference photodiode (reference PD), which is used to record simultaneously a reflectivity image of the SAW device to correlate the displacement maps to the device structure.

Finally, the SAW device is mounted on a three-axes nanopositioning stage, where translation along the optical (z) axis allows one to adjust the focus of the laser beam, while the x and y axes allow one to scan the laser focus over the SAW device. The imaging of the SAW displacement field is done line-by-line with continuous scanning of the x axis of the nanopositioner, simultaneously recording the lock-in signal and the encoder signal of the x translation stage, allowing fast scans with a maximum resolution of ~ 7 nm. An example of such measurement is shown in the bottom panel of Fig. 1(a), where we plot the amplitude of the standing SAWs over a line in the middle of the transverse direction of the SAW cavity, resulting in a spatial x periodicity of half the acoustic wavelength $\Lambda/2$, as expected for standing waves.

We point out that using a single-mode fiber coupler as the beam splitter drastically simplifies the alignment of the interferometer compared to traditional free-space setups [38–42], where perfect mode overlap is hard to achieve. We found that spurious reflections in our fiber-based setup are sufficiently minimized by using exclusively one fiber type and APC (angled physical contact) connectors. To obtain full interference visibility, we only have to match the intensities coupled back from the sample and reference arms, which we do simply by fine-tuning the distance between lens L_1 and the fiber at port C of the interferometer. Also, compared to more complex approaches [33,34], our setup is simpler, more compact, and robust, and because we focus on the device under normal incidence, we can achieve a smaller beam spot size and measure higher-frequency SAWs.

C. Heterodyne circuit

In order to measure the amplitude and phase of the gigahertz SAW displacement, we need to compare the signal at the output of the photodiode to a reference. As a reference, we use the signal from the rf generator in Fig. 1(b), which is the same generator that also drives the IDT in the SAW cavity at a frequency $f_{\mathrm{SAW}} \sim 1$ GHz. The rf generator has a power splitter at its output [not visible in Fig. 1(b)], that allows one to simultaneously drive the IDT and to use the same signal as reference for the heterodyne circuit in Fig. 1(c).

The heterodyne circuit is used to down-convert to a lower frequency the signal from the photodiode and the reference, while maintaining their phase relation. This

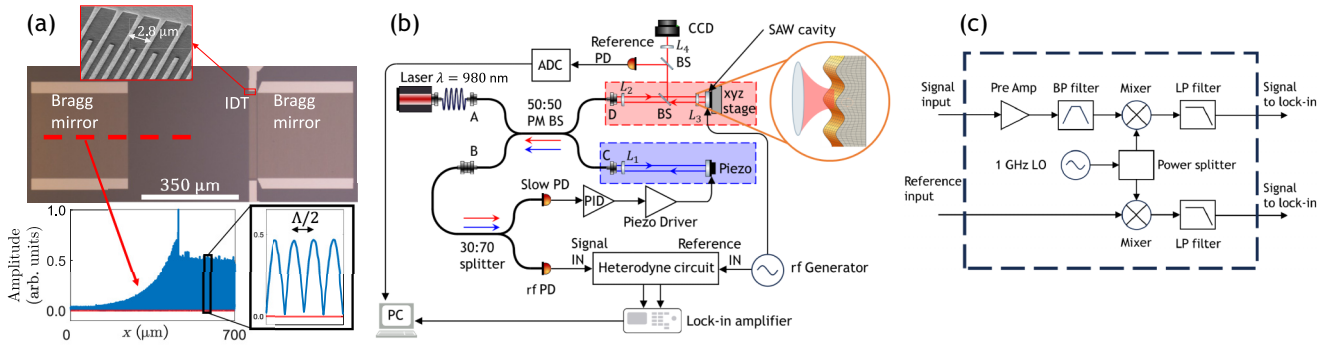


FIG. 1. (a) Optical microscope image of the SAW cavity device, and an electron microscope picture of the IDT metal fingers (top inset). In the bottom panel we show an example of the out-of-plane displacement field, measured with the optical interferometer at the position indicated by the red dashed line. The exponential decay of the field inside the Bragg mirrors is visible, as well as the nodes and antinodes of the standing waves (bottom right). (b) Schematic of the fiber-based scanning optical interferometer. (c) Schematic of the custom-built 1-GHz heterodyne circuit used to convert the 1-GHz SAW signal from the rf photodiode into an intermediate-frequency signal in the range of 1–48 MHz.

lower frequency is called intermediate frequency, and for this conversion we use a local oscillator at a frequency $f_{LO} = f_{SAW} - f_{IF}$, where f_{IF} is the intermediate frequency. The signal generated by the local oscillator is split in two by a power splitter in order to be mixed with the reference and rf photodiode signal. The reference is first mixed with the local oscillator, and then low-pass-filtered, obtaining at the output a reference at the intermediate frequency f_{IF}. On the other hand, the low-amplitude signal from the rf photodiode is preamplified, band-pass-filtered, mixed with the local oscillator, and finally low-pass-filtered, obtaining at the output a signal at the intermediate frequency f_{IF}. These two outputs are then fed into the lock-in amplifier: the output from the reference port constitutes the reference at the intermediate frequency f_{IF}, and is used as an external oscillator in the lock-in amplifier, to demodulate the output coming from the signal port. As a result, the lock-in amplifier can measure the amplitude and phase of the SAW displacement at the intermediate frequency f_{IF}. When we change the drive frequency of the IDT f_{SAW}, we change accordingly also the frequency of the local oscillator f_{LO}, such that the intermediate frequency is kept constant at the arbitrary value of $f_{IF} = 22$ MHz. Because of the bandwidth of the band-pass filter, f_{SAW} is limited to 900–1370 MHz.

D. Voltage-displacement calibration

The voltage signal measured by the lock-in amplifier is converted into the out-of-plane displacement associated to the SAWs by the overall gain of the interferometer:

$$\zeta = \frac{\lambda}{4\pi P_{half}} \frac{1}{C_{rf}\, G_{LI}\, r} \times 10^6 \quad \left[\frac{pm}{\mu V}\right]. \tag{1}$$

Here the first term $4\pi P_{half}/\lambda$ gives the change in the optical power caused by a given flat-surface displacement for an interferometer locked at the side of the fringe, in which λ is the optical wavelength, and $P_{half} = 170$ μW is the optical power at which we side-of-the-fringe lock the interferometer, measured at the rf photodiode. In the second term, $C_{rf} = 700$ V/W is the conversion factor between input optical power and voltage at the output of the rf photodiode, $G_{LI} = 20.6$ is the total voltage gain provided by the heterodyne circuit, and $r = r(w_0, \Lambda)$ is a reduction factor caused by the finite size of the beam waist radius w_0 compared to the acoustic wavelength Λ.

As discussed in Appendix A, the analytical calculation of the reduction factor leads to

$$r(w_0, \Lambda) = \exp\left(-\frac{\pi^2 w_0^2}{2\Lambda^2}\right), \tag{2}$$

showing an exponential dependence on w_0^2. An accurate measurement of the beam waist is therefore essential for a proper calibration, and we measure it by using a variation of the well-known knife-edge technique [45,46], where the focused Gaussian beam is scanned over the boundary between the free GaAs surface and the aluminum contact pad of the IDT.

Because of the two different reflectivities of aluminum and GaAs, in reflection we can measure a transition over this region in the reflected optical power recorded by the reference photodiode, resulting in a measured beam waist radius $w_0 = 1.4$ μm, as shown in Appendix B. In our experiment, the SAW wavelength is $\Lambda = 2.8$ μm, resulting in a reduction factor $r = 0.29$, and a total gain of the interferometer equal to $\zeta = 0.154$ pm/μV rms.

With these parameters, our setup can reliably measure out-of-plane SAW displacements with a sensitivity of 3 pm at a frequency of ~ 1 GHz. This limitation comes from radio-frequency leakage in the heterodyne circuit, where

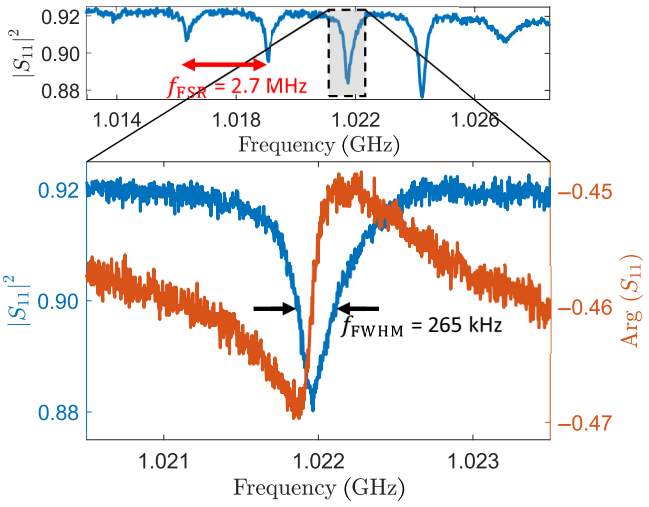


FIG. 2. Microwave reflectance spectrum of the SAW cavity ($|S_{11}|^2$), measured with a VNA. The spectrum shows multiple longitudinal modes separated by a free spectral range $f_{\mathrm{FSR}} = 2.7$ MHz. In the lower panel we show the cavity resonance that is investigated with the optical setup, where the red curve corresponds to the phase of the S_{11} parameter. The measured resonance frequency is $f_c^{\mathrm{VNA}} = 1.02197$ GHz, and the full width at half-maximum is $f_{\mathrm{FWHM}} = 265$ kHz.

part of the signal in the reference input leaks into the input signal path through the power splitter shown in Fig. 1(c).

III. TRANSVERSE MODES IN A PLANAR SAW CAVITY

Here we investigate the planar SAW Fabry-Perot cavity shown in Fig. 1(a). First we characterize the cavity by means of an all-electrical measurement done with a vector network analyzer, then with the interferometric optical setup. By comparison, we show how the latter approach allows for a better understanding of the cavity modes and a better estimation of the cavity parameters. The all-electrical VNA measurement is performed by driving the IDT in the cavity with a vector network analyzer (NANO VNA), and measuring the reflected electrical power. At a resonance of the cavity, there is conversion between electrical energy and mechanical energy, and therefore we expect to observe a dip in the measured reflected power. By performing this measurement at different frequencies, we obtain the microwave reflectance spectrum of the SAW cavity ($|S_{11}|^2$), shown in Fig. 2.

The device shows several resonance frequencies around 1 GHz, with a free spectral range $\Delta f_{\mathrm{FSR}} = 2.7$ MHz, corresponding to an effective cavity length $L_{\mathrm{eff}} = 530$ μm. In the rest of this chapter, we will focus on the third reflection dip, which has a resonance frequency measured by the VNA of $f_c^{\mathrm{VNA}} = 1.02197$ GHz, and shows an asymmetric behavior on the high-frequency side, visible in the lower panel of Fig. 2. This asymmetry in the reflection dip is attributed to the excitation of frequency-overlapping transverse modes, but there is no clear structure corresponding to the individual peaks of these modes.

This is because the IDT cannot distinguish the modes spatially, due to its transverse spatial extension. In fact, at a particular excitation frequency close to the resonance of the fundamental mode, we have the superposition of different cavity modes, each one with a different transverse spatial profile, different amplitude, and different phase. This leads to a complex frequency- and spatially dependent mode superposition, and, since the IDT is extended along the full transverse length of the cavity $L_y = 308$ μm, it measures a spatial average of this mode superposition, which in our case does not show a multipeak structure. We note that in shorter and/or lower-loss SAW cavities, the transverse modes often can be resolved also electrically.

In order to separate these transverse modes in the frequency domain, we measure the SAW cavity with the scanning Michelson interferometer. Since this setup uses a focused laser beam as a small localized probe, we expect the optically measured frequency spectrum to be dependent on the position at which it is measured. Because of placement of the IDT centered to the SAW cavity axis, we expect only symmetrical transverse modes [47]. We drive the IDT with an rf power of 15 dBm, and spatially scan a few periods of the standing waves across the longitudinal z direction of the cavity, recording the peak value of the measured displacement amplitude. The procedure is repeated for different frequencies, allowing us to reconstruct the frequency spectrum of the intracavity field in the middle of the cavity, as shown in Fig. 3(a). In this frequency spectrum, we now recognize several distinct peaks, which correspond to different transverse modes, as we show now.

For this, we use the Michelson interferometer to image the spatial acoustic field distribution inside the SAW cavity for the four peak frequencies f_0–f_3, and we calibrate the measured out-of-plane displacement using Eq. (1). We image a region inside the SAW cavity of 5.6 μm in the longitudinal direction, and 400 μm in the transverse direction. This is shown in Figs. 3(b)–3(e), where we plot both amplitude (left panels) and phase (right panels), and we show the corresponding cross sections with a white curve. For the amplitude maps, the cross section is taken at the position of an antinode, while for the phase maps the cross section is taken at the longitudinal position indicated by the black dashed line.

These maps show transverse field profiles with an odd number of lobes, in our case one, three, five, and seven, corresponding to axially symmetric transverse modes. Moreover, by looking at the amplitude distribution of the acoustic field, it is clear that there is an asymmetry with respect to the center of the transverse direction: not only is the field distribution shifted towards the upper side of the cavity, which is visible especially in Fig. 3(b), but for multilobe modes, the lobe on the bottom side of the cavity has

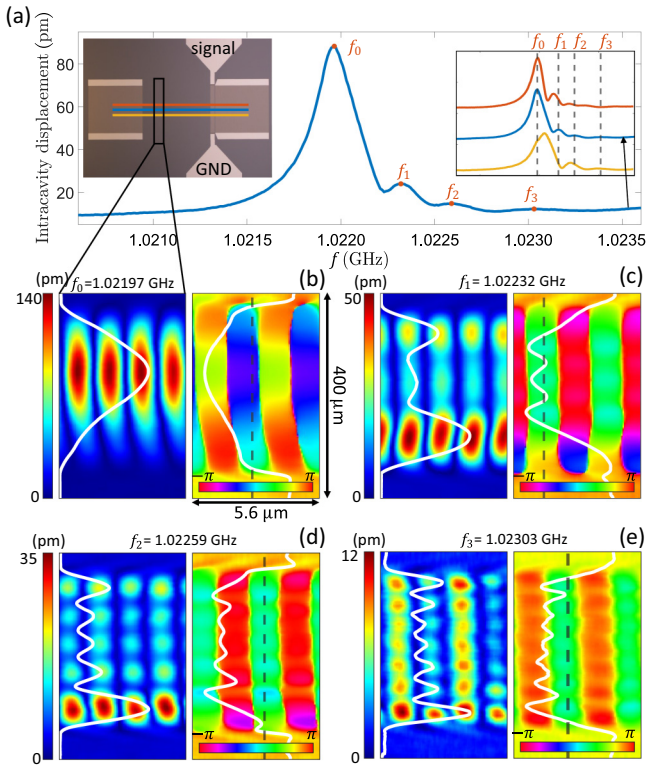


FIG. 3. Optical measurements of the transverse modes. (a) Intracavity out-of-plane displacement as a function of frequency, measured in the middle of the transverse direction of the cavity. In the right inset we show three resonance spectra measured at the different transverse positions indicated in the left inset, demonstrating significant peak shifting and broadening. (b)–(e) Amplitude (left panels) and phase (right panels) of the transverse modes, measured at the indicated peak frequencies, in the area indicated by the black box in panel (a). Each plot has an extension of 400 μm in the transverse direction and 5.6 μm in the longitudinal direction. The different transverse modes are axially symmetric, showing one, three, five, and seven lobes in the transverse direction. The white lines show the cross section of the mode profile measured at the position of an antinode as indicated by the dashed lines in the phase plots.

a higher displacement than the one on the top side. We do not know the origin of this shift and asymmetry.

As mentioned above, due to the presence of the transverse modes, which overlap both in frequency and in space, the optically measured acoustic resonance spectrum depends significantly on the transverse position at which it is measured. This is shown in the right inset of Fig. 3(a), where we measure the acoustic resonance spectrum at different transverse positions indicated by the colored lines in the left inset of Fig. 3(a). From this measurement, it is clear that, due to mode superposition, the resonance spectrum of the displacement shows peaks with different frequency and shape, depending on the transverse position at which is measured. This makes it very hard, if not impossible, to determine accurately the exact resonance frequencies of the different transverse modes, and therefore the acoustic resonance spectrum shown in Fig. 3(b) only gives an estimate of these resonance frequencies.

Another consequence of the mode superposition is that the mode profiles shown in Figs. 3(b)–3(e) do not correspond to transverse normal modes, but are a superposition of multiple modes at the specific frequency at which they are measured. To show this effect, and to show how we can retrieve the *real* mode profile, we now discuss a simple theoretical model with two frequency-overlapping cavity modes M_0 and M_1, corresponding to the fundamental mode and to the first transverse mode. Resonant modes in a cavity are enhanced, with respect to the input field, and the ratio between the enhanced field and the input field is referred to as susceptibility, described by a complex Lorentzian [48],

$$\chi(f) = \frac{1}{1 - 2i(f - f_c)/\Delta f_{\mathrm{FWHM}}}. \tag{3}$$

Here, f_c is the mode frequency, and Δf_{FWHM} its width. The susceptibility is characterized by a π phase shift across a resonance, as shown in Fig. 4(a), where we plot the simulated intracavity field enhancement as a function of frequency for two generic cavity modes M_0 and M_1 with mode frequencies f_0 and f_1. From Fig. 4(a) we see that at the frequency $f = f_0$ the two modes M_0 and M_1 have a phase difference $\Delta\varphi \sim \pi/2$. In the time domain this means that the acoustic field of one mode is described by a cosine oscillation, and the other mode by a sine oscillation.

In our experiment, when driving the acoustic cavity at the frequency f_0, we are exciting not only the fundamental mode M_0 but also the first transverse mode M_1. As a result, the surface oscillation in time is a superposition of sine and cosine functions. Since we are using lock-in quadrature detection to measure the out-of-plane displacement of surface acoustic waves, we can separate the sine and cosine components of the surface oscillations, which are simply given by the X and Y quadratures returned by the lock-in amplifier. Let us now consider the measured field shown in Fig. 3(b), obtained by driving the SAW cavity at the frequency f_0. If we plot the X and Y quadratures instead of the amplitude and phase of the field, we can spatially separate the two mode profiles corresponding to the fundamental mode M_0 and to the first transverse mode M_1. This is shown in Fig. 4(b), where now we can better see the transverse profile of the M_0 and M_1 modes. We note that, in order to obtain this result, we applied a phase shift of $\theta = 1.15$ rad to the data, in order to align the cosine oscillation to the X quadrature.

Another interesting phenomenon caused by mode superposition is the destructive interference of modes M_0 and M_1, visible in Fig. 4(c), where we optically measure the acoustic field distribution at the frequency $f_s =$

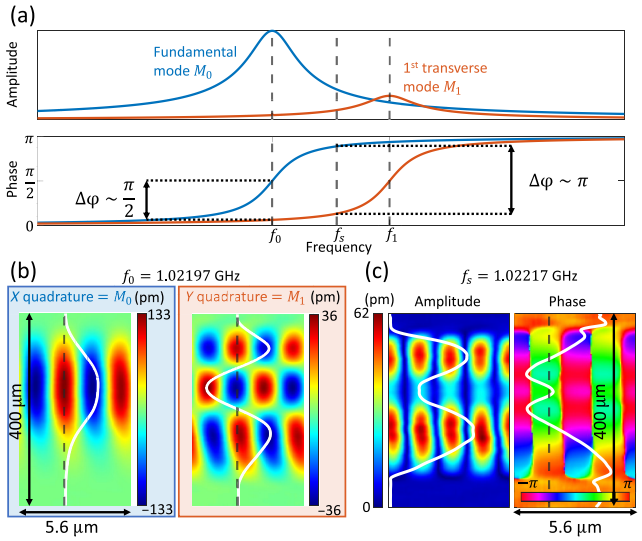


FIG. 4. Mode superpositions. In panel (a) we show the simulated amplitude and phase of two generic frequency-overlapping cavity modes M_0 and M_1. At the resonance frequency f_0 of the fundamental mode M_0, the phase difference is $\Delta\varphi \simeq \pi/2$, and the two modes are almost orthogonal, allowing mode decomposition by quadrature analysis, as shown in panel (b). At the frequency f_s in between f_0 and f_1, the phase difference is $\Delta\varphi \simeq \pi$ and the two modes are almost out of phase with a comparable amplitude, leading to destructive interference and a two-lobe structure, as shown in panel (c).

1.02217 GHz, which is in between f_0 and f_1. From our theoretical model shown in Fig. 4(a), we expect that at the frequency f_s the fields of the two modes M_0 and M_1 now have a phase difference $\Delta\varphi \sim \pi$. This means that the surface oscillation corresponding to the mode M_0 is out of phase with respect to the surface oscillation corresponding to M_1, resulting in destructive interference between the two modes. The result is shown in Fig. 4(c), where the amplitude of the acoustic field distribution shows a two-lobe structure. While in principle this could correspond to an antisymmetric transverse mode, the symmetry observed in the phase is proof that this is indeed a mode superposition between symmetric modes, in our case M_0 and M_1.

Finally, we compare the measured out-of-plane displacement with the estimated surface displacement that we expect for the fundamental mode of the planar SAW cavity. For this estimation, we first calculate the steady-state phonon number $\bar{n}$ starting from the definition of cavity quality factor that takes into account the stored energy:

$$Q = 2\pi f_0 \frac{E_s}{P_{\text{loss}}}, \tag{4}$$

where E_s is the energy stored in the cavity, and P_{loss} is the power loss. At steady state, the stored energy is $E_s = \bar{n}\, h f_0$, where h is the Planck constant, and the power loss must be equal to the input power in the cavity $P_{\text{in}} = \eta\, P_{\mu\text{wave}}$, where η is the fraction of power coupled to the cavity, and $P_{\mu\text{wave}}$ is the rf power sent to the IDT.

The quality factor can also be described in term of the linewidth of the resonator $Q = f_0/f_{\text{FWHM}}$, where f_{FWHM} is the width at half-maximum of the cavity resonance. By comparing this definition to Eq. (4), we can obtain the steady-state phonon number

$$\bar{n} = \frac{\eta\, P_{\mu\text{wave}}}{h f_0} \frac{1}{2\pi f_{\text{FWHM}}}. \tag{5}$$

From the microwave reflectance spectrum $|S_{11}|^2$, we estimate $\eta = 0.04$ and $f_{\text{FWHM}} = 265$ kHz. The rf microwave power sent to the IDT is $P_{\mu\text{wave}} = 15$ dBm, obtaining $\bar{n} = 1.1 \times 10^{15}$. We can convert the steady-state phonon number into a SAW displacement, by using the relation $u = u_{\text{zpm}}\sqrt{\bar{n}}$, where u_{zpm} is the zero-point motion, and for SAWs on GaAs it has been numerically estimated to be $u_{\text{zpm}} \simeq 1.9\ \text{fm}/\sqrt{A\ [\mu\text{m}^2]}$ [19], where A is the surface area on which the mode is confined, expressed in μm^2. We estimate $A = L_{\text{eff}} \times L_{\text{FWHM}} \simeq 9 \times 10^4\ \mu\text{m}^2$, where $L_{\text{eff}} = v_{\text{SAW}}/(2f_{\text{FSR}}) = 530\ \mu\text{m}$ is the effective cavity length corresponding to the free spectral range $f_{\text{FSR}} = 2.7$ MHz of our cavity as measured in Fig. 2, and $L_{\text{FWHM}} = 170\ \mu\text{m}$ is the FWHM of the SAW field profile along the transverse direction in Fig. 3(b).

With these cavity parameters, we obtain an estimate of the SAW peak displacement of $u \simeq 210$ pm, which is of the same order of magnitude as the optically measured value $u_{\text{meas}} = 140$ pm in Fig. 3(b). We note that the estimated SAW peak displacement is an overestimation of the real value, since we assumed that all the input power P_{in} dissipated in the IDT goes into excitation of the acoustic waves, whereas in reality there are also Ohmic losses due to the finite resistance of the IDT, metal bus bars, and wire bonds.

IV. CONCLUSIONS AND OUTLOOK

We presented a fiber-based Michelson interferometer which, combined with a heterodyne circuit, enables frequency- and spatially resolved measurements of the amplitude and phase of surface-acoustic-wave displacements. We used this setup to investigate transverse modes in a 1-GHz SAW cavity, revealing the presence of higher-order transverse modes which were not resolved in all-electrical measurements. First, by imaging the acoustic fields, we show that the transverse modes overlap in frequency and space, leading to mode superpositions. This modifies both the acoustic resonance spectrum of the cavity and the spatial profile of the modes. Second, we show that the mode superposition can be decomposed into normal modes by quadrature analysis. The combination of frequency measurements and spatial imaging enables a more complete characterization of SAW cavities, and of SAW devices in general, and can play a crucial role in optimization of SAW devices.

ACKNOWLEDGMENTS

We would like to thank H. Visser for helping with the heterodyne circuit and for useful discussions. We acknowledge funding from NWO/OCW (QUAKE, 680.92.18.04; Quantum Software Consortium, No. 024.003.037), from the Dutch Ministry of Economic Affairs (Quantum Delta NL), and from the European Union's Horizon 2020 research and innovation program under Grant Agreement No. 862035 (QLUSTER).

APPENDIX A: EFFECTS OF THE BEAM SPOT SIZE ON THE MEASURED INTERFEROMETRIC SIGNAL

We discuss here the effects of the optical beam spot size on the measured interferometric signal, for which we need to keep in mind the optical interferometer sketched in Fig. 1(b). The gain of the interferometer provided in Eq. (1) has been calculated by taking into account the change in the optical power at the photodiode, caused by the displacement of a reflective flat surface in the sample arm of the interferometer. The effect of the beam spot size is incorporated into the reduction factor $r(w_0, \Lambda)$.

We can calculate this reduction factor by comparing the fluctuations in the optical power at the photodiode, caused by reflection from an oscillating flat surface (P^{Ω}_{flat}), to the fluctuations caused by reflection from the oscillating SAW surface (P^{Ω}_{SAW}), where Ω is the angular frequency of oscillation. Since the heterodyne detection system detects the rms values of the optical power fluctuations, we introduce $P^{\text{rms}}_{\text{flat}}$ and $P^{\text{rms}}_{\text{SAW}}$, and define the reduction factor as

$$r = \frac{P^{\text{rms}}_{\text{SAW}}}{P^{\text{rms}}_{\text{flat}}}, \tag{A1}$$

where $P^{\text{rms}}_{\text{SAW}}$ and $P^{\text{rms}}_{\text{flat}}$ denote the rms value of P^{Ω}_{SAW} and P^{Ω}_{flat}, respectively.

We now proceed to calculate these two fluctuations in the optical power. Looking at Fig. 1(b), first we calculate the electric field coupled back into the fiber in both the reference and sample arms of the interferometer, where the field in the sample arm is modulated in phase by the oscillating surface. Then we let the two fields interfere and we keep only the Ω component in the optical power fluctuation. Starting from the reference arm, since the interferometer is locked at half of the interference fringe, we define a reference field with unitary amplitude and constant phase $E_{\text{ref}} = \exp(i\pi/2)$.

In the sample arm of the interferometer, we want to calculate the field back-reflected into port D of the fiber coupler for the two cases of SAW oscillations and oscillations of a flat surface. This field is given by the overlap integral between the field supported by the optical fiber, and the field reflected by the oscillating reflective surface. Since optical propagation is unitary, we can calculate this integral at any plane in the sample arm of the interferometer, and for simplicity we choose the plane of the reflecting surface. Here the overlap integral is calculated between the image of the field supported by the fiber E_{fiber} and the reflected fields E_{flat} and E_{SAW}.

In the interferometer we can achieve close-to-unity coupling back to the fiber. Therefore, we can assume that the image of E_{fiber} at the reflecting surface has the same beam waist as the focused laser beam, leading to $E_{\text{fiber}} = \exp[-(x^2+y^2)/w_0^2]$. The reflected fields can be expressed as a generic Gaussian beam with an additional phase term picked upon reflection from the oscillating surface:

$$\begin{aligned} E &= \frac{2}{\pi w_0^2} \exp\left(-\frac{x^2+y^2}{w^2(z)}\right) \\ &\quad \times \exp\left[-i\left(2k(z+\Delta z) + k\frac{x^2+y^2}{2R(z)} - \psi(z)\right)\right] \\ &\simeq \frac{2}{\pi w_0^2} \exp\left(-\frac{x^2+y^2}{w_0^2}\right) \exp\left(-2ik\Delta z\right). \end{aligned} \tag{A2}$$

Here we drop the constant propagating phase z, and the phase terms corresponding to the Gouy phase $\psi(z)$ and to the radius of curvature $R(z)$. This approximation is valid for small surface displacements close to the focus. We can then write $E_{\text{flat}} = E_{\text{fiber}} \exp(-2ik\Delta z_{\text{flat}})$ and $E_{\text{SAW}} = E_{\text{fiber}} \exp(-2ik\Delta z_{\text{SAW}})$.

Let us first consider the flat case, for which the surface displacement is given by $\Delta z_{\text{flat}} = A_0 \cos(\Omega t)$, where A_0 is the peak surface displacement, and Ω is the angular frequency of the surface oscillation. The field coupled back to port D of the fiber coupler is given by

$$\begin{aligned} E'_{\text{flat}} &= \iint E^*_{\text{fiber}} E_{\text{flat}}\, dx\, dy \\ &= \frac{2}{\pi w_0^2} \iint \exp\left(-2\frac{x^2+y^2}{w_0^2}\right) \exp[-2ik\Delta z_{\text{flat}}]\, dx\, dy \\ &= \exp(-2ik\Delta z_{\text{flat}}). \end{aligned} \tag{A3}$$

The total power at the photodiode is given by the interference of E'_{flat} with E_{ref}:

$$\begin{aligned} P_{\text{flat}} &= |E'_{\text{flat}} + E_{\text{ref}}|^2 \\ &= \left|\exp\left(i\frac{\pi}{2}\right) + \exp(-2ikA_0\cos(\Omega t))\right|^2 \\ &\simeq 2 + 4kA_0\cos(\Omega t) + 4k^2A_0^2\cos^2(\Omega t), \end{aligned} \tag{A4}$$

where we have expanded for small displacements A_0. Keeping in mind that the rms value of a time signal is

defined as

$$P_{\mathrm{rms}} = \sqrt{\frac{1}{T}\int_0^T P^2(t)\,dt}, \tag{A5}$$

we obtain the rms value of the Ω component $P_{\mathrm{flat}}^{\mathrm{rms}} = 4kA_0/\sqrt{2}$.

We now repeat the same calculations for E_{SAW}, i.e., not assuming a flat reflecting surface. In this case, the position-dependent surface displacement is given by

$$\begin{aligned}\Delta z_{\mathrm{SAW}} &= A_C \cos(\Omega t)\cos[K(x-x_0)] \\ &\quad + A_S \sin(\Omega t)\sin[K(x-x_0)],\end{aligned} \tag{A6}$$

which is the sum of two time-shifted standing waves, with peak displacement A_C and A_S, respectively. The surface displacement written in this form is a superposition of traveling and standing waves along the x direction, depending on the amplitudes A_C and A_S. In the above equation, $K = 2\pi/\Lambda$ is the SAW wave number, Ω is the angular frequency, and x_0 is the transverse position of the laser beam on the SAW device.

We now carry out the calculations by considering this generic displacement, and in the end we can separate between the case of purely traveling waves by imposing $A_C = A_S = A_0$, and purely standing waves by imposing $A_S = 0$ and $A_C = A_0$. In this way, the standing waves are defined such that, at position $x_0 = 0$, the laser beam is focused on an antinode, and where A_0 is the peak surface displacement. The field that couples back to the fiber is now given by

$$\begin{aligned}E'_{\mathrm{SAW}} &= \iint E^*_{\mathrm{fiber}} E_{\mathrm{SAW}}\,dx\,dy \\ &= \iint E^2_{\mathrm{fiber}} \exp(-2ik\Delta z_{\mathrm{SAW}}).\end{aligned} \tag{A7}$$

Because of the small SAW displacement, we can expand the exponential containing Δz_{SAW}, and we can ignore all terms containing $\sin(Kx)$ since they are even functions and their integration is zero. The overlap integral therefore becomes

$$\begin{aligned}E'_{\mathrm{SAW}} &= \frac{2}{\pi w_0^2}\int \exp\left(-\frac{2y^2}{w_0^2}\right)dy \\ &\quad \times \int \exp\left(-\frac{2x^2}{w_0^2}\right)[1 - 2ik\gamma\cos(Kx)]\,dx,\end{aligned} \tag{A8}$$

where $\gamma = A_c\cos(\Omega t)\cos(Kx_0) - A_S\sin(\Omega t)\sin(Kx_0)$. The integral can be solved by expanding the cosine term $\cos(Kx) = [\exp(iKx) + \exp(-iKx)]/2$, and using the standard integral:

$$\int_{-\infty}^{+\infty} \exp(-ax^2 + ibx)\,dx = \sqrt{\frac{\pi}{a}}\exp\left(-\frac{b^2}{4a}\right). \tag{A9}$$

The result is given by

$$E'_{\mathrm{SAW}} \simeq 1 + 2ik\gamma e^{-B}, \tag{A10}$$

where $B = -K^2 w_0^2/8$.

Similarly to what we did in Eq. (A4), we calculate the total power at the photodiode, resulting in the interference of E'_{SAW} and E_{ref}:

$$P_{\mathrm{SAW}} = 2 - 4\gamma e^{-B} + 4k^2\gamma^2 e^{-2B}. \tag{A11}$$

The Ω component of the optical power at the photodiode for a SAW displacement is given by

$$P_{\mathrm{SAW}}^{\Omega} = 4k\gamma e^{-B}. \tag{A12}$$

Now, before we calculate the rms value, we need to separate the case of traveling and standing waves. For traveling waves, we impose $A_C = A_S = A_0$, which results in $\gamma = A_0[\cos(\Omega t)\cos(Kx_0) - \sin(\Omega t)\sin(Kx_0)]$. We then obtain $P_{t\mathrm{SAW}}^{\mathrm{rms}} = 4kA_0\exp(-B)/\sqrt{2}$, where the subscript t stands for traveling. For the case of standing SAW waves, we impose $A_S = 0$ and $A_C = A_0$, obtaining $\gamma = A_0\cos(\Omega t)\cos(Kx_0)$, and the rms change in the optical power is given by $P_{s\mathrm{SAW}}^{\mathrm{rms}} = P_{t\mathrm{SAW}}^{\mathrm{rms}}|\cos(Kx_0)|$, where the subscript s stands for standing wave. The measured rms change in the Ω component of the optical power caused by traveling SAWs is therefore equivalent to that caused by standing SAWs, measured when the laser is on an antinode ($x_0 = 0$). By comparing this result with the rms change in the optical power caused by the displacement of a flat surface, we obtain the wanted reduction factor r:

$$r = \frac{P_{\mathrm{SAW}}^{\mathrm{rms}}}{P_{\mathrm{flat}}^{\mathrm{rms}}} = \exp\left(-\frac{K^2 w_0^2}{8}\right). \tag{A13}$$

In our case, $\Lambda = 2.8$ μm and $w_0 = 1.4$ μm, resulting in $r = 0.29$, as shown in Fig. 5, where we plot the reduction factor and we show our experimental conditions. The total gain of the interferometer in Eq. (1) is therefore $\zeta = 0.154$ pm/μV rms.

APPENDIX B: BEAM SPOT SIZE MEASUREMENT

As discussed in the main text, the sine-like shape of the displacement generated by a SAW affects the reduction factor $r = \exp(-K^2 w_0^2/8)$. Because of the exponential dependence on the beam waist radius, an accurate measurement of w_0 is crucial for a proper calibration of the

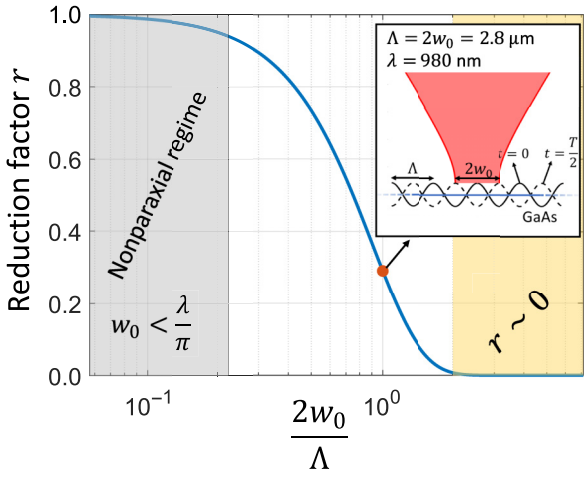


FIG. 5. Reduction factor. The blue curve is the reduction factor from Eq. (2), as a function of the ratio between laser beam spot $2w_0$, and the acoustic wavelength Λ of SAWs. The red dot indicates our experimental conditions, with $\Lambda = 2w_0 = 2.8\ \mu m$, and optical wavelength $\lambda = 980$ nm. The gray shaded area on the left with $w_0 < \lambda/\pi$ corresponds to the nonparaxial regime, where our calculation of the reduction factor is not valid. The yellow shaded area on the right with $2w_0/\Lambda > 2$ corresponds to a region where $r \sim 0$. The inset panel shows a sketch of the experiment, in which we show the surface profile at time $t = 0$ and $t = T/2$, corresponding to half the oscillation period of the standing waves.

measured voltage into a displacement. We perform this measurement *in situ*, using a variation of the knife-edge technique. Here we use the boundary between the GaAs substrate and the metal contact pad of the SAW cavity IDT as a knife edge. We shine a focused laser beam on the sample, move the sample along the x direction, and, using the reference photodiode in Fig. 1(b), measure the reflected power over the boundary between the GaAs and Al. An example of such measurement is shown in Fig. 6.

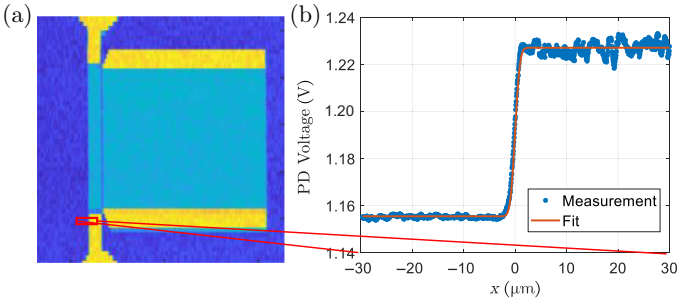


FIG. 6. Measurement of the beam spot size with a variation of the knife-edge technique. (a) Image of the IDT and Bragg mirror metal structure, obtained with the reference photodiode in Fig. 1(b). (b) Photodiode voltage (blue) as a function of x position, and fitted function (red), according to Eq. (B1).

In a reference frame where the boundary coincides with the origin of the x axis, the reflected power is

$$P = P_0 \left[r_2 + r_1 + (r_2 - r_1)\,\mathrm{erf}\left(\frac{x\sqrt{2}}{w_0}\right)\right], \qquad \text{(B1)}$$

where P_0 is the optical power of the incident beam (in arbitrary units), r_1 is the reflection coefficient for GaAs, r_2 is the reflection coefficient for Al, and w_0 is the beam waist radius. Figure 6 shows the region over which such measurement has been performed, the measured data, and the fitting function. The fitted parameters are $w_0 = 1.4\ \mu m$ and $r_1 = 0.30$. The expected reflection coefficient of GaAs at $\lambda \simeq 1\ \mu m$ is $r_{GaAs} = 0.3097$, which is in very good agreement with the fitted r_1.

[1] S. G. Joshi and R. M. White, Excitation and detection of surface elastic waves in piezoelectric crystals, J. Acoust. Soc. Am. **46**, 17 (1969).

[2] R. M. White and F. W. Voltmer, Direct piezoelectric coupling to surface elastic waves, Appl. Phys. Lett. **7**, 314 (1965).

[3] P. Delsing, *et al.*, The 2019 surface acoustic waves roadmap, J. Phys. D: Appl. Phys. **52**, 353001 (2019).

[4] B. Paschke, A. Wixforth, D. Denysenko, and D. Volkmer, Fast surface acoustic wave-based sensors to investigate the kinetics of gas uptake in ultra-microporous frameworks, ACS Sens. **2**, 740 (2017).

[5] Z. Chen, J. Zhou, H. Tang, Y. Liu, Y. Shen, X. Yin, J. Zheng, H. Zhang, J. Wu, X. Shi, Y. Chen, Y. Fu, and H. Duan, Ultrahigh-frequency surface acoustic wave sensors with giant mass-loading effects on electrodes, ACS Sens. **5**, 1657 (2020).

[6] J. W. Grate, Acoustic wave microsensor arrays for vapor sensing, Chem. Rev. **100**, 2627 (2000).

[7] K. Länge, B. E. Rapp, and M. Rapp, Surface acoustic wave biosensors: A review, Anal. Bioanal. Chem. **391**, 1509 (2008).

[8] F. Guo, P. Li, J. B. French, Z. Mao, H. Zhao, S. Li, N. Nama, J. R. Fick, S. J. Benkovic, and T. J. Huang, Controlling cell–cell interactions using surface acoustic waves, Proc. Natl. Acad. Sci. **112**, 43 (2015).

[9] D. J. Collins, B. Morahan, J. Garcia-Bustos, C. Doerig, M. Plebanski, and A. Neild, Two-dimensional single-cell patterning with one cell per well driven by surface acoustic waves, Nat. Commun. **6**, 8686 (2015).

[10] T. Franke, S. Braunmüller, L. Schmid, A. Wixforth, and D. A. Weitz, Surface acoustic wave actuated cell sorting (SAWACS), Lab Chip **10**, 789 (2010).

[11] T. Takai, H. Iwamoto, Y. Takamine, H. Yamazaki, T. Fuyutsume, H. Kyoya, T. Nakao, H. Kando, M. Hiramoto, T. Toi, M. Koshino, and N. Nakajima, High-performance SAW resonator on new multilayered substrate using $LiTaO_3$ crystal, IEEE Trans. Ultrason. Ferroelectr. Freq. Contr. **64**, 1382 (2017).

[12] K.-Y. Hashimoto, *Surface Acoustic Wave Devices in Telecommunications* (Springer, Berlin, Heidelberg, 2000).
[13] K. Yang, C. He, J. Fang, X. Cui, H. Sun, Y. Yang, and C. Zuo, Advanced RF filters for wireless communications, Chip **2**, 100058 (2023).
[14] R. Manenti, A. F. Kockum, A. Patterson, T. Behrle, J. Rahamim, G. Tancredi, F. Nori, and P. J. Leek, Circuit quantum acoustodynamics with surface acoustic waves, Nat. Commun. **8**, 975 (2017).
[15] M. V. Gustafsson, T. Aref, A. F. Kockum, M. K. Ekström, G. Johansson, and P. Delsing, Propagating phonons coupled to an artificial atom, Science **346**, 207 (2014).
[16] B. A. Moores, L. R. Sletten, J. J. Viennot, and K. W. Lehnert, Cavity quantum acoustic device in the multimode strong coupling regime, Phys. Rev. Lett. **120**, 227701 (2018).
[17] K. J. Satzinger, Y. P. Zhong, H. -S. Chang, G. A. Peairs, A. Bienfait, M. -H. Chou, A. Y. Cleland, C. R. Conner, É. Dumur, J. Grebel, I. Gutierrez, B. H. November, R. G. Povey, S. J. Whiteley, D. D. Awschalom, D. I. Schuster, and A. N. Cleland, Quantum control of surface acoustic-wave phonons, Nature **563**, 661 (2018).
[18] M. Weiß and H. J. Krenner, Interfacing quantum emitters with propagating surface acoustic waves, J. Phys. D: Appl. Phys. **51**, 373001 (2018).
[19] M. J. A. Schuetz, E. M. Kessler, G. Giedke, L. M. K. Vandersypen, M. D. Lukin, and J. I. Cirac, Universal quantum transducers based on surface acoustic waves, Phys. Rev. X **5**, 031031 (2015).
[20] R. A. DeCrescent, Z. Wang, P. Imany, R. C. Boutelle, C. A. McDonald, T. Autry, J. D. Teufel, S. W. Nam, R. P. Mirin, and K. L. Silverman, Large single-phonon optomechanical coupling between quantum dots and tightly confined surface acoustic waves in the quantum regime, Phys. Rev. Appl. **18**, 034067 (2022).
[21] M. Metcalfe, S. M. Carr, A. Muller, G. S. Solomon, and J. Lawall, Resolved sideband emission of InAs/GaAs quantum dots strained by surface acoustic waves, Phys. Rev. Lett. **105**, 037401 (2010).
[22] Y. Sato, J. C. H. Chen, M. Hashisaka, K. Muraki, and T. Fujisawa, Two-electron double quantum dot coupled to coherent photon and phonon fields, Phys. Rev. B **96**, 115416 (2017).
[23] R. Manenti, M. J. Peterer, A. Nersisyan, E. B. Magnusson, A. Patterson, and P. J. Leek, Surface acoustic wave resonators in the quantum regime, Phys. Rev. B **93**, 041411 (2016).
[24] R. Takasu, Y. Sato, T. Hata, T. Akiho, K. Muraki, and T. Fujisawa, Surface-acoustic-wave resonators with Ti, Cr, and Au metallization on GaAs, Appl. Phys. Express **12**, 055001 (2019).
[25] T. Luschmann, A. Jung, S. Geprägs, F. X. Haslbeck, A. Marx, S. Filipp, S. Gröblacher, R. Gross, and H. Huebl, Surface acoustic wave resonators on thin film piezoelectric substrates in the quantum regime, Mater. Quantum. Technol. **3**, 021001 (2023).
[26] M. E. Msall and P. V. Santos, Focusing surface-acoustic-wave microcavities on GaAs, Phys. Rev. Appl. **13**, 014037 (2020).
[27] I. S. Camara, B. Croset, L. Largeau, P. Rovillain, L. Thevenard, and J. -Y. Duquesne, Vector network analyzer measurement of the amplitude of an electrically excited surface acoustic wave and validation by X-ray diffraction, J. Appl. Phys. **121**, 044503 (2017).
[28] J. Hellemann, F. Müller, M. Msall, P. V. Santos, and S. Ludwig, Determining amplitudes of standing surface acoustic waves via atomic force microscopy, Phys. Rev. Appl. **17**, 044024 (2022).
[29] P. A. Goddard, G. F. Clark, B. K. Tanner, and R. W. Whatmore, Stroboscopic synchrotron-X-radiation topography and its application to the imaging of travelling surface acoustic waves, Nucl. Instrum. Methods Phys. Res. **208**, 705 (1983).
[30] J.-D. Nicolas, T. Reusch, M. Osterhoff, M. Sprung, F. J. R. Schülein, H. J. Krenner, A. Wixforth, and T. Salditt, Time-resolved coherent X-ray diffraction imaging of surface acoustic waves, J. Appl. Crystallogr. **47**, 1596 (2014).
[31] M. Hanke, N. Ashurbekov, E. Zatterin, M. Msall, J. Hellemann, P. Santos, T. Schulli, and S. Ludwig, Scanning X-ray diffraction microscopy of a 6-GHz surface acoustic wave, Phys. Rev. Appl. **19**, 024038 (2023).
[32] J. Gualtieri and J. Kosinski, Large-area, real-time imaging system for surface acoustic wave devices, IEEE Trans. Instrum. Meas. **45**, 872 (1996).
[33] R. Hisatomi, K. Taga, R. Sasaki, Y. Shiota, T. Moriyama, and T. Ono, Quantitative optical imaging method for surface acoustic waves using optical path modulation, Phys. Rev. B **107**, 165416 (2023).
[34] A. Iwasaki, D. Nishikawa, M. Okano, S. Tateno, K. Yamanoi, Y. Nozaki, and S. Watanabe, Temporal-offset dual-comb vibrometer with picometer axial precision, APL Photonics **7**, 106101 (2022).
[35] H. Kamizuma, L. Yang, T. Omori, K.-y. Hashimoto, and M. Yamaguchi, High-speed laser probing system for surface acoustic wave devices based on knife-edge method, Jpn. J. Appl. Phys. **44**, 4535 (2005).
[36] K. Taga, R. Hisatomi, Y. Ohnuma, R. Sasaki, T. Ono, Y. Nakamura, and K. Usami, Optical polarimetric measurement of surface acoustic waves, Appl. Phys. Lett. **119**, 181106 (2021).
[37] B. D. Rummel, L. Miroshnik, M. Patriotis, A. Li, T. R. Sinno, M. D. Henry, G. Balakrishnan, and S. M. Han, Imaging of surface acoustic waves on GaAs using 2D confocal Raman microscopy and atomic force microscopy, Appl. Phys. Lett. **118**, 031602 (2021).
[38] J. V. Knuuttila, P. T. Tikka, and M. M. Salomaa, Scanning Michelson interferometer for imaging surface acoustic wave fields, Opt. Lett. **25**, 613 (2000).
[39] K. Kokkonen and M. Kaivola, Scanning heterodyne laser interferometer for phase-sensitive absolute-amplitude measurements of surface vibrations, Appl. Phys. Lett. **92**, 063502 (2008).
[40] A. Gollwitzer, A. Lerner, and G. Fischerauer, in *2006 IEEE International Frequency Control Symposium and Exposition* (IEEE, Miami, FL, USA, 2006), p. 424.
[41] K.-Y. Hashimoto, K. Kashiwa, N. Wu, T. Omori, M. Yamaguchi, O. Takano, S. Meguro, and K. Akahane, A laser probe based on a Sagnac interferometer with fast mechanical scan for RF surface and bulk acoustic wave devices,

IEEE Trans. Ultrason. Ferroelectr. Freq. Control. **58**, 187 (2011).

[42] H. Takahashi, T. Omori, and K.-Y. Hashimoto, Development of a high-speed, phase-sensitive laser probe system for RF surface acoustic wave/bulk acoustic wave devices with an absolute vibration amplitude measurement function, Jpn. J. Appl. Phys. **60**, SDDC10 (2021).

[43] W. Haydl, B. Dischler, and P. Hiesinger, in *1976 Ultrasonics Symposium* (IEEE, Annapolis, MD, USA, 1976), p. 287.

[44] Y. Yamamoto and S. Yoshimoto, in *1998 IEEE Ultrasonics Symposium. Proceedings (Cat. No. 98CH36102)* (IEEE, Sendai, Japan, 1998), Vol. 1, p. 229.

[45] J. A. Arnaud, W. M. Hubbard, G. D. Mandeville, B. de la Clavière, E. A. Franke, and J. M. Franke, Technique for fast measurement of Gaussian laser beam parameters, Appl. Opt. **10**, 2775 (1971).

[46] D. R. Skinner and R. E. Whitcher, Measurement of the radius of a high-power laser beam near the focus of a lens, J. Phys. E: Sci. Instrum. **5**, 237 (1972).

[47] C. Campbell, Modelling the transverse-mode response of a two-port SAW resonator, IEEE Trans. Ultrason. Ferroelect. Freq. Contr. **38**, 237 (1991).

[48] M. Aspelmeyer, T. J. Kippenberg, and F. Marquardt, Cavity optomechanics, Rev. Mod. Phys. **86**, 1391 (2014).